RSC Advances

PAPER

View Article Online
View Journal | View Issue

Cite this: *RSC Adv.*, 2025, **15**, 5413

Design of acidic activation-responsive charge-switchable carbon dots and validation of their antimicrobial activity†

Zhuo Li,‡[a] Hui Li,‡[a] Zhenrong Tang,[b] Qingxia Tang,[c] Chang Liao,[a] Hua Tang *[a] and Dan Wang *[d]

Bacterial biofilms play a crucial role in the emergence of antibiotic resistance and the persistence of chronic infections. The challenge of effectively eradicating bacterial biofilms while ensuring minimal toxicity to normal cells persists. Carbon-based artificial nanoenzymes have attracted considerable attention as emerging nanotheranostic agents, owing to their biocompatibility, cost-effectiveness, and straightforward synthesis. In this study, we have developed a multifunctional carbon dots (CDs) system, specifically CDs functionalized with 1-(3-aminopropyl) imidazole (API), termed CDs-API. This system demonstrates acid-activated antibiofilm activity. The CDs-API were synthesized from chlorogenic acid (ChA), a bioactive compound naturally occurring in coffee, and subsequently functionalized with API to achieve charge-switchable properties under acidic conditions. This distinctive feature enables CDs-API to efficiently penetrate bacterial biofilms and selectively target the colonized bacteria. The enzyme-like activity of CDs-API effectively consumes high levels of glutathione (GSH) within the biofilm, leading to the accumulation of reactive oxygen species (ROS). Consequently, this process degrades the extracellular polymeric substance (EPS) matrix, damages bacterial DNA and protein structures, and disrupts the redox balance, ultimately leading to bacterial cell death. Experimental results demonstrated that CDs-API effectively inhibited the growth of methicillin-resistant *Staphylococcus aureus* (MRSA) and *Pseudomonas aeruginosa* (PAE) while promoting wound healing with minimal damage to healthy tissues. The acid-activated charge-switchable capability of CDs-API provides superior antibacterial efficacy compared to traditional antibiotics, rendering it a promising candidate for the treatment of bacterial biofilm infections.

Received 8th January 2025
Accepted 5th February 2025

DOI: 10.1039/d5ra00174a

rsc.li/rsc-advances

Introduction

The World Health Organization (WHO) has highlighted antimicrobial resistance (AMR) as a critical threat to global public health, with projections indicating that, by 2050, mortality attributable to AMR could exceed that of cancer.[1,2] The exacerbation of this issue is driven by the misuse of antibiotics and the paucity of novel antimicrobial agents.[3–5] Compounding these challenges, bacteria are capable of forming biofilms, complex three-dimensional colonies encased in an extracellular polymeric substance (EPS), which significantly impede conventional treatment methodologies.[6–9] Currently, effective strategies for targeting biofilm-associated infections are limited, highlighting the urgent necessity for innovative approaches to address the escalating threat posed by drug-resistant bacteria.[10,11] Owing to their potent efficacy and broad-spectrum antimicrobial properties, nanomaterial-based antimicrobial therapies have emerged as increasingly promising options for the treatment of bacterial infections and biofilm-related drug resistance in recent years.[12,13] To evaluate their efficacy, various nanomaterials exhibiting properties have been synthesized and

[a]*Key Laboratory of Molecular Biology for Infectious Diseases (Ministry of Education), Chongqing Medical University, Chongqing 400010, China. E-mail: tanghua86162003@cqmu.edu.cn; cqwangdan61@163.com*

[b]*Department of Breast and Thyroid Surgery, The First Affiliated Hospital of Chongqing Medical University, Chongqing 400010, China*

[c]*Clinical Laboratory, The People's Hospital of Rongchang District, Chongqing 402460, China*

[d]*Post-Doctoral Research Center, The People's Hospital of Rongchang District, Chongqing 402460, China*

† Electronic supplementary information (ESI) available: Fig. S1, characterization of ChA CDs and CDs-API. Fig. S2, absorbance changes of ChA CDs upon different GSH concentrations (1, 2, 3, and 4 mM). Fig. S3, MIC evaluation of CDs-API. Fig. S4, plates colony plots after treatment with various groups on other pathogenic bacteria. Fig. S5, results of crystal-violet-stained biofilm and biofilm biomass of MRSA and PAE with different treatment groups. Fig. S6, cell viability tests of HUVECs under various CDs-API concentration. Fig. S7, growth of MRSA and PAE in LB medium from the infected wound secretions on the sixth day. Fig. S8, wound healing area ratio–time curves for MRSA-infected and PAE-infected mice groups. Fig. S9, growth of MRSA and PAE on LB agar from the infected wound secretions at the end of different treatments. Fig. S10, body weight changes in MRSA-infected and PAE-infected mice groups. Fig. S11, H&E staining of major organs from mice after 12 days of different treatments. See DOI: https://doi.org/10.1039/d5ra00174a

‡ Zhuo Li and Hui Li have contributed equally to this work.

employed in both *in vivo* and *in vitro* studies.[14–16] Within the domain of antimicrobial research, metal-based nanomaterials (including gold, silver, titanium oxide, and zinc oxide) have shown considerable potential.[17–20] However, the non-specific biotoxicity associated with these potent antibacterial metal-based nanoparticles has limited their clinical application.[21,22]

Carbon quantum dots (CDs), a subset of the nanomaterials utilized in the antimicrobial sector, are gaining increase recognition due to their extensive functionalization capabilities, high water solubility, ease of synthesis, and superior biocompatibility.[23–25] Over the past decade, CDs have experienced significant growth in biological applications due to their nanoscale size (1–10 nm), unique optical properties, and ease of functionalization.[26–30] The synthesis of CDs has predominantly employed two methodologies: "top-down" and "bottom-up" approaches.[31–36] Previous studies have demonstrated the versatility and effectiveness of CDs in various biomedical applications, including imaging and therapeutic platforms.[37,38] An increasing body of research indicates that CDs-based nanomaterials can mimic the structure and function of natural enzymes, leading to oxidative stress damage in biological membrane systems through the accumulation of ROS.[39–42] Concurrently, CDs exhibit greater biocompatibility with normal organisms compared to the biotoxicity associated with metal-based nanoparticles.[43] Additionally, their diminutive size enhances biofilm penetration by allowing them to traverse various natural biological barriers within the body.[44]

Chlorogenic acid (ChA), a naturally occurring polyphenolic compound, exhibits a broad spectrum of biological activities, including antiviral, antibacterial, and ROS scavenging properties.[45] ChA is known for its excellent biocompatibility and potent antioxidant properties, making it an ideal candidate for synthesizing CDs with enhanced biological activity. Yao *et al.*[46] employed a hydrothermal technique, inspired by the intense roasting of coffee, to synthesize ChA CDs which demonstrated significant glutathione-like activity. By reducing glutathione (GSH) levels, they have the potential to disrupt cellular redox homeostasis, leading to oxidative stress and cell death. Notably, these low-toxicity CDs retained their negative charge. While they do lessen harm to normal cells and attain improved biocompatibility, their antibacterial efficacy and biofilm permeability were less than that of positively charged nanomaterials.[47] The accumulation of EPSs facilitates anaerobic bacterial fermentation within the biofilm, resulting in an acidic internal environment.[48,49] Researches have demonstrated that the surface charge of the nanomaterials transitions from negative to positive upon entering this acidic milieu, thereby enhancing their ability to penetrate the biofilm.[50–53] Consequently, these nanoparticles exhibit increased efficacy in eradicating drug-resistant bacteria residing within the biofilm.[54–58]

In this study, ChA served as the precursor, while 1-(3-aminopropyl) imidazole (API) functioned as the surface modifier. The API comprises an imidazole ring and a propyl chain terminated with an amino group ($-NH_2$). Its simple structure enables the formation of stable amide bonds with the carboxyl groups on ChA CDs, thereby facilitating straightforward surface modification while preserving the ultrasmall size of ChA CDs. In acidic environments, API quickly reverse their charge to positive due to the protonation of the imidazole groups ($pK_a \approx 6.8$). Conversely, under alkaline conditions, it undergoes deprotonation, reverting to a neutral state.[59,60] By harnessing these pH-sensitive charge conversion properties, the imidazole group functions as a donor to modify the ChA CDs, ultimately leading to the formation of CDs-API. The CDs-API exhibited remarkable enzyme-like activities and environmentally responsive charge-switching capabilities, which enabled significant penetration of biofilms and effective eradication of deeply colonized bacteria, all while maintaining excellent biocompatibility (Scheme 1). This modification in surface charge has been shown to possess significant antibacterial activity both *in vitro* and *in vivo*, contributing to the healing of wounds infected with bacteria. The antibacterial activity of CDs strongly correlates with their nitrogen content and surface charges.[61] Compared to other charge-switchable nanomaterials,[48–50] CDs-API achieve their charge-switchable capability through a straightforward surface modification process. This uncomplicated modification enables them to maintain the bactericidal efficacy of positive charges while ensuring exceptional biofilm penetration ability and preserving high biocompatibility in healthy tissues. Our study highlights the remarkable novelty and benefits of CDs-API, particularly in tackling biofilm-related challenges that traditional antibiotics fail to address effectively. Consequently, CDs-API emerges as a highly promising candidate for the treatment of bacterial biofilm infections.

Materials and methods

Materials and reagents

ChA, 1-(3-dimethylaminopropyl)-3-ethylcarbodiimide hydrochloride (EDC), *N*-hydroxysuccinimide (NHS), 2-morpholinoethanesulfonic acid (MES), potassium chloride (KCl), 3,3′-di(propylthiocarbocyanine) iodide ($diSC_3(5)$), acridine orange (AO), ethidium bromide (EB) and sodium chloride (NaCl) were obtained from Shanghai Aladdin (China). Sodium hydroxide (NaOH) was supplied by National Pharmaceutical Chemical Reagents (China). API and propidium iodide (PI) were acquired from Sigma-Aldrich (USA). Crystal violet, methanol and ethanol were provided by Chron (Chengdu, China). Luria Bertani (LB) bacterial culture medium was supplied by Sangon Biotech (Shanghai, China). Phosphate-buffered saline (PBS), ATP analysis kit, GSH analysis kit and MTT assay kit were provided by Beyotime Biotech (Shanghai, China). Dulbecco's Modified Eagle Medium (DMEM) was provided by Saimike (Chongqing, China). Aqueous solutions were prepared using Milli-Q water (18.2 MΩ, Millipore, USA).

MRSA (ATCC 43300), PAE (ATCC 27853), *Klebsiella pneumoniae* (*K. pneumoniae*), *Escherichia coli* (*E. coli*, ATCC 25922) and extended-spectrum beta-lactamase (ESBLs)-producing *Klebsiella pneumoniae* (ESBLs-producing *K. pneumoniae*) were obtained from the People's Hospital of Rongchang District (Chongqing, China).

Synthesizing CDs-API

ChA CDs were synthesized utilizing a conventional one-step hydrothermal method. Specifically, 150 mg of ChA was

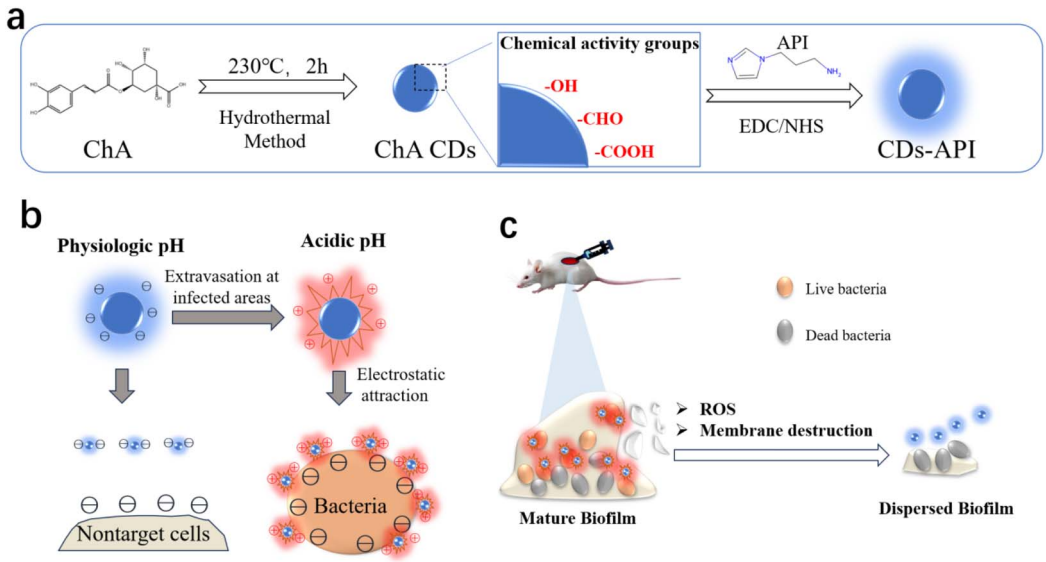

Scheme 1 Schematic illustration of (a) the synthesis process of CDs-API and its mechanism of antimicrobial activity *in vitro* (b) and *in vivo* (c).

dissolved in 30 mL of ultrapure water and subsequently transferred to a PTFE-lined autoclave reactor. The mixture was then subjected to a thermal reaction in an oven preheated to 230 °C for a duration of 2 h. Following the reaction, the solution was allowed to cool to room temperature, filtered through a 0.02 μm membrane, and dialyzed with a 1 kDa dialysis bag for 8 h. The resulting brownish-yellow aqueous solution of ChA CDs was either stored at 4 °C in the dark, or lyophilized as required. Subsequently, the ChA CDs were utilizing the EDC/NHS method. Specifically, 50 mg of EDC and 25 mg of NHS were dissolved in 1 mL of MES buffer (pH 5.5). Following this, 2 mL of ChA CDs were added to the solution and incubated for 1 h at 37 °C. Thereafter, 1 mL of API was introduced, and the pH of the mixture was adjusted to 8. The resulting mixture was incubated at 4 °C overnight. Dialysis was conducted using a 3 kDa dialysis bag for a duration of 24 h, with the water being replaced every 2 h. Finally, the CDs-API complex was freeze-dried to yield a yellowish solid powder, which was subsequently stored at 4 °C in the dark. The zeta potentials of ChA CDs and CDs-API were measured in both neutral and acidic environments.

Verification of charge switchable capability

The zeta potentials of ChA CDs and CDs-API were measured in both neutral and acidic environments by dynamic light scattering (DLS). A 1 mg mL^{-1} solution of ChA CDs and a 1 mg mL^{-1} solution of CDs-API were prepared respectively, and the zeta potentials of these nanomaterials were measured across a pH ranging from 5.0 to 7.4 at 25 °C.

Validation of glutathione-like enzyme activity

The glutathione peroxidase-like peroxidase catalytic activity of ChA CDs and CDs-API were assessed by using the glutathione peroxidase assay kit (DTNB assay). Specifically, ChA CDs or CDs-API was firstly diluted to a concentration of 1 mg mL^{-1} in PBS. DTNB solution (100 μM) and varying concentrations of GSH solution (1 mM, 2 mM, 3 mM, 4 mM) were then added to the diluted ChA CDs or CDs-API solution. The mixtures were co-incubated at room temperature, and absorbance values were detected at 412 nm at different incubation times (0 min, 10 min, 20 min, 30 min, and 40 min).

Bacterial culture

MRSA and PAE were chosen as model organisms to evaluate the antimicrobial efficacy of CDs-API. The absorbance of the bacterial solution at a wavelength of 600 nm (OD_{600}) was periodically measured using a spectrophotometer to monitor bacterial growth. Upon reaching an absorbance value of 0.5, the bacterial concentration was approximately 10^8 CFU mL^{-1}, signifying that the bacteria were in the logarithmic growth phase.

Antibacterial activity assay *in vitro*

The antimicrobial activity of the materials was determined with the agar plate counting method. The MRSA and PAE strains were cultured in LB broth and agitated separately at 220 rpm for 3 h in a 37 °C incubator to reach the logarithmic growth phase. The bacterial solutions were then diluted with PBS (0.01 M, pH 7.4) to achieve a bacterial concentration of approximately 10^6 CFU mL^{-1}. ChA CDs and CDs-API were prepared as a 1 mg mL^{-1} solutions in PBS. Subsequently, 100 μL of each solution was dispensed into a 96-well plate, followed by the addition of 100 μL of bacterial suspension. The mixtures were incubated for 20 min at room temperature. Thereafter, 100 μL of each sample was spread onto LB agar plates, allowed to stand for 10 min, and then inverted and incubated at 37 °C for 18 h. Growth monitored, and colony counts were performed. Concurrently, 5 μL of the sample from each well was added to 5 mL of LB liquid medium and incubated overnight at 37 °C with shaking at

200 rpm. OD_{600} was measured using a spectrophotometer the following day.

Live-dead cell staining

To evaluate the effect of CDs-API on bacteria, log-phase cultures of MRSA and PAE were prepared. The bacterial suspensions (10^8 CFU mL^{-1}) were centrifuged at 8000 rpm for 3 min, then washed three times with PBS to remove any residual culture medium. Next, 500 μL of the bacterial suspension was mixed with 100 μL of ChA CDs or CDs-API (1 mg mL^{-1}) and incubated for 20 min, PBS was used as the control group. Following this, 60 μL of the AO/EB solution was added to the bacterial mixture and incubated in the dark for 15 min to stain the bacteria. After staining, the samples were washed three times with PBS to remove excess dye. Finally, the bacteria were resuspended in PBS, and 10 μL of the suspension was placed on a microscope slide for fluorescence imaging using a confocal laser scanning microscope (CLSM).

Minimum inhibitory concentration (MIC) determination

MRSA and PAE strains were cultured in LB liquid medium and grown to the logarithmic phase in a constant temperature shaker at 37 °C. The bacterial suspension was then diluted with PBS (0.01 M, pH 7.4) to achieve a bacterial load of approximately 10^6 CFU mL^{-1}. ChA CDs and CDs-API were prepared in PBS at various concentrations (final concentrations of 0.2, 0.3, 0.4, 0.6, 0.8 and 1 mg mL^{-1}, respectively). A volume of 100 μL of PBS, ChA CDs, and CDs-API solutions were dispensed into 96-well plates, followed by the addition of 100 μL of the prepared bacterial suspensions to each well. The mixtures were then incubated at room temperature for 20 min. Subsequently, the same procedures as those employed in the *in vitro* antimicrobial activity assay were conducted to observe bacterial growth in each group using LB liquid medium and LB agar plates.

Broad-spectrum antimicrobial activity assay

E. coli, *K. pneumoniae*, and ESBLs-producing *K. pneumoniae* were selected as model organisms to evaluate the broad-spectrum antimicrobial efficacy of CDs-API *in vitro*. Single colonies were isolated from agar plates and inoculated into screw-top tubes containing LB liquid medium. These cultures were then incubated at 37 °C with shaking at 200 rpm for 3 h to reach the logarithmic growth phase ($OD_{600} = 0.5$). Subsequently, 100 μL of PBS, ChA CDs and CDs-API (1 mg mL^{-1}) were each combined with 100 μL of the bacterial solutions in a 96-well plate. The mixtures were gently agitated and incubated at room temperature for 20 min. 10 μL of each mixture was spread onto LB agar plates, which were then inverted and incubate at 37 °C overnight. Photographs were taken the following day to document colony growth.

Biofilm disruption capacity testing *in vitro*

The extent of bacterial biofilm disruption was assessed using crystalline violet (CV) dye. Initially, 200 μL each of MRSA and PAE bacterial solutions (approximately 10^8 CFU mL^{-1}) were dispensed into sterile 96-well plates and incubated at 37 °C for 36 h to facilitate biofilm formation. Following the aspiration of the bacterial suspension, the wells were rinsed with PBS to eliminate non-adherent bacteria. Subsequently, PBS, CDs, or CDs-API solutions (1 mg mL^{-1}) was added to each well and incubated at 37 °C for 3 h. The supernatant was then aspirated, and 200 μL of 0.1% CV dye was added, followed by a 15 min incubation period protected from light. The wells were washed three times with PBS, and 200 μL of 95% ethanol was added to solubilize the CV dye. Finally, the biofilm content was quantified by measuring OD_{590}.

Observation of biofilm morphology

To investigate the effects of CDs-API on biofilm morphology, both CLSM and microscopy (SEM) were employed. For SEM observation, glass slides were placed in 24-well plates, 1 mL each of MRSA culture at 10^8 CFU mL^{-1} was added into the 24-well plate per well and incubated at 37 °C for 36 h to facilitate biofilm formation. Subsequently, ChA CDs or CDs-API (1 mg mL^{-1}) were added to the biofilm cultures and incubated at 37 °C for 30 min, with PBS used as a control group. The samples were washed with PBS and then air-dry the glass slides. The biofilms formed on the glass slides were fixed in 2.5% glutaraldehyde solution at 4 °C for 24 hours, followed by washing with PBS, fixation with osmium tetroxide, dehydration using a gradient ethanol series (30%, 50%, 70%, 90%, 95%, and 100%) at room temperature for 10 min each, and vacuum drying. Samples were then coated with conductive material and observed using SEM. Biofilms formed on the glass slides were treated with the above method, stained with AO for 30 min, followed by gentle washing three times with PBS to remove excess dye. Then imaged by CLSM to obtain a 3D structure.

Observation of bacterial morphology

The surface morphology of bacteria subjected to different treatments was observed using SEM. Bacterial cultures of PAE and MRSA (10^8 CFU mL^{-1}) were collected and incubated with PBS (0.01 M, pH 7.4), ChA CDs (1 mg mL^{-1}), or CDs-API (1 mg mL^{-1}) for 20 min, respectively. Subsequently, bacterial precipitates were obtained by centrifugation at 5000 rpm for 3 min. The excess medium was removed by washing with PBS, and the collected bacterial precipitates were resuspended in a 2.5% glutaraldehyde solution. The bacteria were fixed at 4 °C for 24 h and then were dehydrated in different concentrations of ethanol (50%, 70%, 80%, 90%, 100%) for 10 min, dried under vacuum conditions, coated with gold, visualized and photographed using SEM.

Bacterial membrane system damage validation

The fluorescent dye PI was employed as an indicator of altered bacterial membrane permeability. 500 μL each of MRSA and PAE bacterial suspensions (10^6 CFU mL^{-1}) were prepared. To each suspension, CDs-API solutions (1 mg mL^{-1}) were added, followed by incubation at 37 °C for 1 h and 2 h, respectively. 50 μM of PI fluorescent probe solution was added, and OD_{535} was measured. The potential alterations in the phospholipid bilayer

of bacterial cell membranes were assessed by monitoring the charge-dependent aggregation release of $diSC_3(5)$. 800 μL each of MRSA and PAE (10^6 CFU mL^{-1}) were utilized, to which 60 μL $diSC_3(5)$ (4 μM) and 60 μL KCl (100 mM) were added, followed by co-incubate at room temperature for 1 h. Subsequently, CDs-API solutions (1 mg mL^{-1}) were added to the respective samples, followed by incubation at 37 °C for 1 h and 2 h, respectively. OD_{620} was then measured.

Bacterial metabolic level studies

MRSA and PAE bacterial suspensions (10^6 CFU mL^{-1}) were mixed with PBS, ChA CDs (1 mg mL^{-1}), and CDs-API (1 mg mL^{-1}), respectively, and incubated for 30 min. Bacterial cells were lysed using bacterial lysate on ice, and the supernatant was collected by centrifugation at 12 000*g* for 5 min. In a sterile 96-well plate, 100 μL of ATP working solution was added to each well and incubated at room temperature for 5 min, 100 μL of CDs-API solution (1 mg mL^{-1}) was then added and gently mixed. The chemiluminescence values were measured.

ROS signal detection

The single linear oxygen fluorescent probe 9,10-anthracenyl-bis (methylene) dicarboxylic acid (ABDA) was employed to quantify the ROS. 50 μL of ABDA solution (500 mM) was mixed with (i) MRSA (10^8 CFU mL^{-1}) + ChA CDs (1 mg mL^{-1}), PAE (10^8 CFU mL^{-1}) + ChA CDs (1 mg mL^{-1}); (ii) MRSA (10^8 CFU mL^{-1}) + CDs-API (1 mg mL^{-1}), PAE (10^8 CFU mL^{-1}) + CDs-API (1 mg mL^{-1}) were mixed and co-incubated at room temperature, and OD_{378} was measured at different times (10 min, 20 min, 30 min, 40 min).

Cytotoxicity assays *in vitro*

Human umbilical vein endothelial cells (HUVECs) were selected for the *in vitro* cytotoxicity study. Cell viability was assessed using the MTT assay. 10 μL of MTT (0.5 mg mL^{-1}) was added to each well, and incubated for 4 h. The supernatant was aspirated, followed by the addition of 100 μL of DMSO, and the wells were agitated for 10 min. OD_{490} was then measured.

Antimicrobial activity assay *in vivo*

According to the "3R" principle (reduction, replacement, refinement), 6 week-old female BALB/c mice were randomly assigned to either MRSA-infected or PAE-infected groups. Each group was further subdivided into three subgroups ($n = 3$), which were as follows: PBS blank control group, ChA CDs treatment group, and CDs-API treatment group. Briefly, the backs of the mice were depilated, and a circle with a diameter of approximately 9 mm was marked at a fixed location using a hole punch. Under ether gas anesthesia, a designated circular area of skin on the backs of the mice was excised using surgical scissors. Subsequently, 100 μL of MRSA bacterial solution and PAE bacterial solution (10^8 CFU mL^{-1}) were applied to the exposed wound site. After 24 h of individual housing, visible pus formation at the wound site confirmed the successful establishment of septic skin infections. Treatments with PBS (0.01 M, pH 7.4), ChA CDs (1 mg mL^{-1}), and CDs-API (1 mg mL^{-1}) were administered directly to the wounds at a dosage of 50 μL per mouse. Throughout the treatment period, the drugs were administered at regular intervals, and changes in wound size were meticulously recorded on a daily basis. Mouse weight was monitored bi-daily. On the twelfth day, mice were euthanized, and pus samples were collected from the infected site. These samples were diluted with PBS, inoculated in LB liquid medium and agar plates, and incubated at 37 °C for 18 h, to observe colony growth. Tissue samples, including the dorsal wound, surrounding skin, and major organs (heart, liver, spleen, lungs, and kidneys), were excised and fixed in 4% paraformaldehyde for 48 h. Subsequently, the tissues were dehydrated, embedded in paraffin, sectioned into 4–6 μm thick slices, stained with hematoxylin and eosin (H&E), and imaged using a panoramic scanning system to evaluate histological features.

Results and discussion

Characterization of CDs-API

In this work, ChA CDs were synthesized *via* a hydrothermal reaction. To endow the ChA CDs with charge-switching capabilities in acidic environments, surface modification was performed using a small molecule API. Transmission electron microscopy (TEM) images showed that the shape of CDs-API was similar to that of ChA CDs, with a size of approximately 2.51 nm (Fig. S1a and b†). The high-resolution TEM (HRTEM) showed a lattice spacing of 0.22 nm for the CDs-API, consistent with a typical graphene structure (Fig. 1a). X-ray diffraction (XRD) pattern also indicated the presence of graphitic carbon in CDs-API (Fig. 1b). Furthermore, the UV-vis absorption of API, ChA CDs and CDs-API were also measured. As shown in Fig. S1c,† the UV-vis spectrum of ChA CDs displayed two distinct broad peaks, centered at 260 nm and 330 nm, respectively. These peaks could be ascribed to the π–π* transition of an aromatic π system and the n–π* transition of carbonyl groups, aligning with observations noted in various CDs synthesized through different methodologies.[24,25] In contrast, the spectrum of CDs-API exhibited two primary absorption peaks approximately at 280 nm and 330 nm, which correspond to the characteristic absorptions of API and ChA CDs, respectively.

The surface functional groups of CDs-API were further characterized using X-ray photoelectron spectroscopy (XPS) and Fourier transform infrared (FT-IR). XPS analysis revealed that ChA CDs were predominantly composed of carbon and oxygen elements. Subsequent grafting of the API onto the surface of ChA CDs resulted in the detection of nitrogen (Fig. 1c). The high-resolution XPS (HR-XPS) spectrum of the C 1s and N 1s were meticulously fitted, In the C 1s orbit of CDs-API, the binding energy peaks located at 284.8 eV, 285.97 eV, and 287.89 eV were attributed to the existence of C–C, C–O, and C=O bonds, respectively. These findings align well with those observed in the C 1s orbit of ChA CDs, suggesting the presence of various functional groups, such as –OH and –COOH, on the surface of both ChA CDs and CDs-API. (Fig. S1d and e†). Additionally, in the N 1s orbit of CDs-API, the peaks at 400.01 eV and

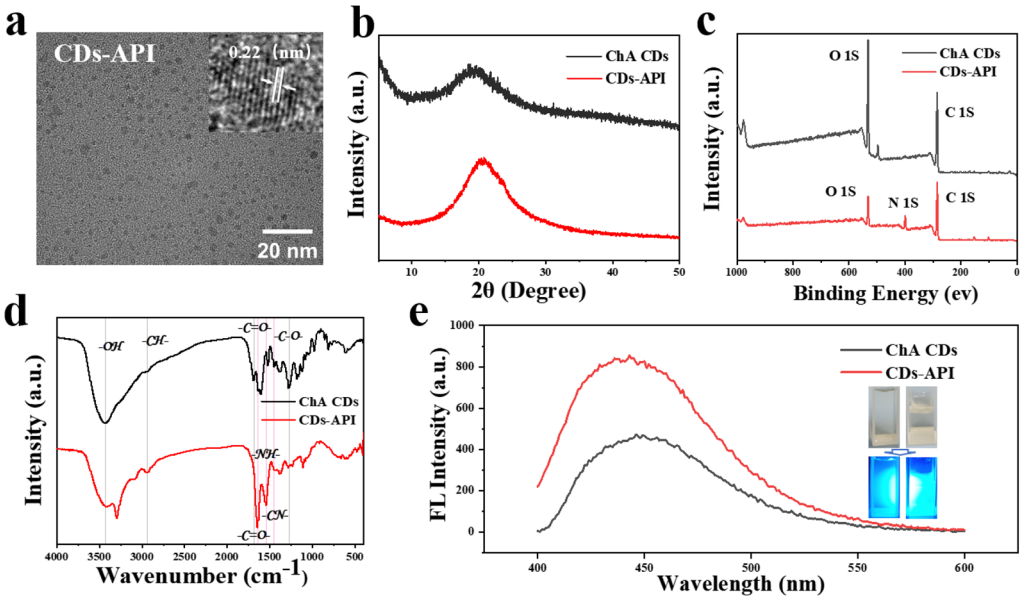

Fig. 1 Characterization of CDs-API. (a) TEM image of CDs-API. Inset: HRTEM image. (b) XRD pattern of ChA CDs and CDs-API. (c) XPS survey spectrum of ChA CDs and CDs-API. (d) FT-IR Spectra of ChA CDs and CDs-API. (e) Fluorescence spectra of ChA CDs and CDs-API measured with excitation at 370 nm and emission scamming at 400–600 nm. Inset: bright-field and UV fluorescent images of ChA CDs (left) and CDs-API (right).

399 eV correspond to the amide bond and imine bond, respectively, indicating the successful formation of an amide linkage (Fig. S1f†). FT-IR spectroscopy identified characteristic peaks at 1545 cm^{-1} and 1448 cm^{-1}, which were attributed to the stretching vibrations of N–H and C–N bonds in the amide linkages (Fig. 1d). Consistent with prior studies, both ChA CDs and CDs-API demonstrated excellent photoluminescence properties (Fig. 1e). The observed enhancement in fluorescence intensity indicated that the fluorescent characteristics of CDs might be associated with their surface functional groups.

Performance validation of CDs-API

Previous researches have suggested that ChA CDs possess the potential to mimic glutathione peroxidase (GPX) activity. This enzymatic activity facilitates the consumption of GSH by ChA CDs, resulting in the accumulation of ROS, which subsequently induces oxidative stress damage in bacteria. This mechanism suggests a potential application for CDs as antibacterial agents. To verify the GPX-like activity of the synthesized CDs-API, we assessed the GSH consumption efficiency utilizing the DTNB assay. The results demonstrated that the absorbance of the solution incubated with CDs-API varied over time and with different GSH concentrations, indicating effective GSH consumption by CDs-API (Fig. 2a). The API modification did not change the GPX-like activity of ChA CDs, further supporting their potential application as effective antibacterial agents (Fig. S2†).

Infection sites are frequently characterized by an acidic environment with elevated GSH levels. The acid-triggered charge-reversal mechanism not only enhances the delivery of CDs-API to healthy tissues but also promotes their accumulation within biofilms. This further augments the antibacterial efficacy of CDs-API and is crucial for eradicating bacteria colonizing biofilms. To confirm the pH-responsive charge conversion properties of CDs-API, the zeta potential was measured across different pH environments (Fig. 2b). At pH 7.5, both ChA CDs and CDs-API exhibited negative charges. However, in an acidic environment with pH $\leq$ 5.5, the surface charge of CDs-API reversed to positive. This charge reversal was attributed to the protonation of the imidazolyl groups on the surface of CDs-API.

Antibacterial performance of CDs-APIs *in vitro*

By integrating the benefits of switchable surface charge, ultra-small size, high dispersibility in aqueous solutions, and exceptional GSH consumption capability, CDs-API exhibits substantial potential as an effective antibacterial agent. To evaluate the antibacterial activity of CDs-API, we performed an assessment of the inhibitory effects on MRSA and PAE using the plate count method. The results indicated that, at equivalent concentrations, CDs-API exhibited significantly stronger antibacterial effects compared to ChA CDs (Fig. 3a). Additionally, the OD_{600} of LB liquid culture medium under various treatments was measured. Statistical analysis confirmed that the inhibitory effect of CDs-API on bacterial growth was consistent with the results obtained from the plate assay (Fig. 3b and c). AO/EB dyes were employed to stain bacteria treated with PBS, ChA CDs, and CDs-API. As illustrated in Fig. 3d and e, bacteria in the PBS group predominantly exhibited green fluorescence, while the CDs-API group displayed almost exclusively red fluorescence, demonstrating that CDs-API significantly disrupted the bacterial cell membranes. Within the concentration range of 0 to 1 mg mL^{-1}, the growth inhibition of MRSA and PAE increased with the concentration of CDs-API (Fig. S3†). The MIC

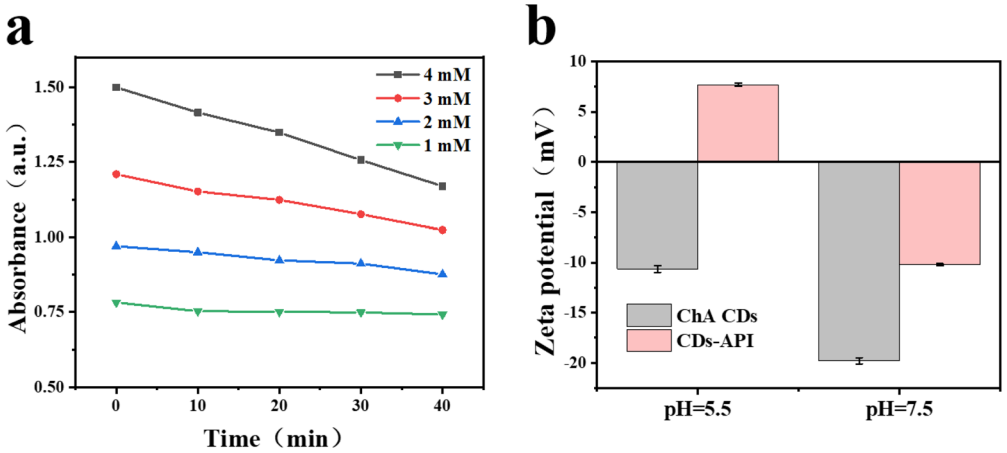

Fig. 2 Performance validation of CDs-API. (a) Absorbance of CDs-API upon the addition of different GSH concentrations (1, 2, 3, and 4 mM). (b) ζ-Potential of ChA CDs and CDs-API.

of CDs-API for both MRSA and PAE was determined to be 1 mg mL^{-1}, achieving an inhibition rate exceeding 99%. Moreover, CDs-API also exhibited excellent and stable broad-spectrum antibacterial activity against clinically prevalent strains such as *E. coli*, *K. pneumoniae*, and ESBLs-producing *K. pneumoniae*, indicating its potential as a promising candidate for the treatment of chronic and complex infections (Fig. S4†). Compared to standard clinical antibiotics, CDs-API achieved complete bacterial inhibition within 20 minutes of incubation, underscoring its rapid bactericidal efficacy.

Anti-biofilm capability of CDs-API *in vitro*

To evaluate the impact of CDs-API on mature biofilms, we observed the microscopic morphology of the MRSA and PAE biofilms. As depicted in Fig. 4a, the OD_{590} values of the CDs-API group were significantly lower than that of the PBS group, indicating the disruption of biofilms. Simultaneously, we conducted a series of concentration gradient tests and found that, at the MIC concentration, CDs-API already demonstrates potent anti-biofilm activity. In contrast, ChA CDs, albeit exhibiting concentration-dependent anti-biofilm activity, demonstrated significantly lesser efficacy at lower concentrations in

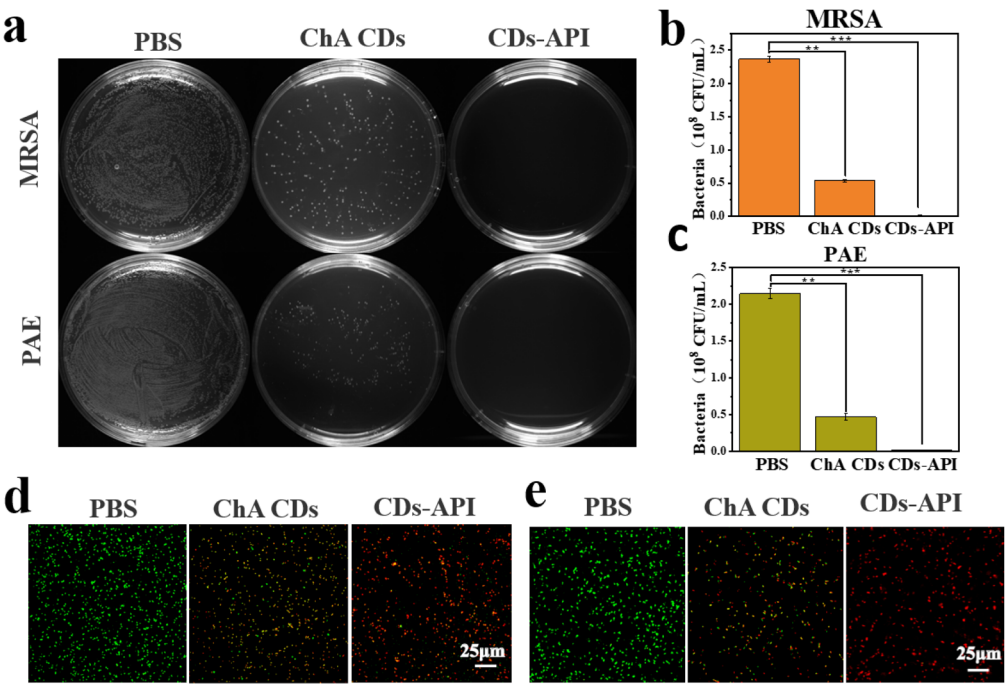

Fig. 3 Antibacterial performance evaluation of CDs-API *in vitro*. (a) Plates colony plots after treatment with various groups. Statistical analyses of MRSA (b) and PAE (c) growth in LB medium after different treatments. Fluorescence images of MRSA (d) and PAE (e) stained with AO and EB after different treatments (scale bar: 25 μm) (**p < 0.01, ***p < 0.001).

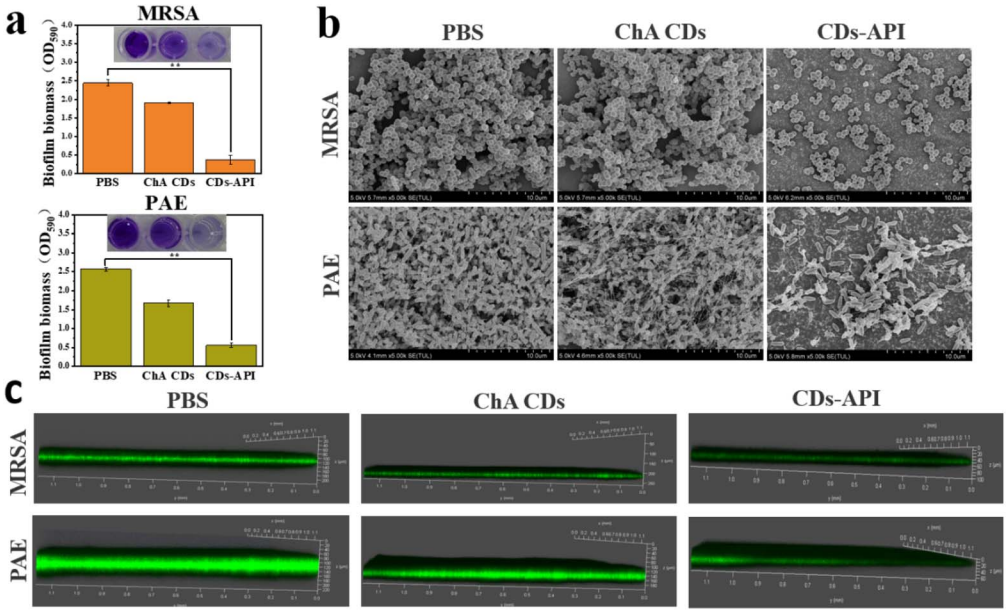

Fig. 4 Anti-biofilm activity of CDs-API *in vitro*. (a) Biofilm elimination in MRSA and PAE under the influence of PBS, ChA CDs and CDs-API, respectively. (b) SEM images of MRSA and PAE biofilms after different treatments (scale bar: 10 μm). (c) CLSM images of MRSA and PAE biofilms after different treatments. Each group of nanoparticles at the concentration of 1 mg mL^{-1}.

comparison to CDs-API. This underscores the superior efficiency of CDs-API in disrupting mature biofilms (Fig. S5†).

SEM images and AO staining intuitively demonstrated the destructive effects of CDs-API on biofilms. As show in Fig. 4b, after treatment with CDs-API, the biofilm structure became loose, with significantly reduced bacterial cell aggregation. The overall thickness of the biofilm is markedly reduced, and some areas completely expose the underlying surface. The presence of minimal EPS and cellular debris further suggest the collapse of the biofilm structure. AO staining corroborated these observations (Fig. 4c): compared to other groups, the CDs-API group had the thinnest biofilms and the weakest fluorescence intensity. This enhanced biofilm disruption was likely attributable to the improved biofilm penetration capability conferred by the environmentally responsive charge conversion properties of CDs-API. These results indicated that CDs-API possesses significant biofilm disruption capability *in vitro*.

Antibacterial performance of CDs-API *in vivo*

To further evaluate the biomedical potential of CDs-API, cytotoxicity tests were performed using HUVECs. HUVECs were incubated with varying concentrations of CDs-API. The results demonstrated that even at a concentration of 10 mg mL^{-1}, there was no significant reduction in cell viability (Fig. S6†). To evaluate the *in vivo* antibacterial efficacy and wound healing properties of CDs-API, an experiment was conducted using a mice model. A 9 mm circular wound was uniformly created on the dorsal surface of the mice, and the wounds were subsequently inoculated with MRSA or PAE bacterial suspensions to induce infection. The successfully infected mice were randomly assigned to three groups: a PBS control group, a ChA CDs treatment group, and a CDs-API treatment group ($n = 3$). Treatments were administered concurrently each day for a duration of 12 days (Fig. 5a). By the 6th day of treatment, the PBS control group displayed pronounced edema and ulceration at the wound sites, whereas the wounds in the ChA CDs and CDs-API treatment groups were significantly reduced in size and exhibited signs of crusting and healing (Fig. 5b and c). At this juncture, pus samples from the wounds of each group were collected and cultured in LB liquid medium. After an 18 hour incubation period, the bacterial suspension in the PBS group exhibited marked turbidity, in contrast to the suspensions in the ChA CDs and CDs-API groups, which remained clear and transparent. This observation suggested that bacterial growth was effectively inhibited by the 6th day of treatment (Fig. S7†). Throughout the treatment duration, wounds in the PBS group exhibited progressive degradation, indicative of ongoing bacterial proliferation. Conversely, wounds in the ChA CDs and CDs-API groups demonstrated gradual crust formation and healing, with a significant reduction in wound area over time. Notably, the CDs-API group demonstrated notably faster healing efficiency compared to the other groups (Fig. S8†). By the conclusion of the treatment period, wounds in the CDs-API group were nearly fully healed, exhibiting a more rapid healing rate compared to those in the ChA CDs group. Bacterial suspensions from the infected wound sites of each group were cultured on LB agar plates. Notably, the ChA CDs and CDs-API groups exhibited minimal formation of single colonies (Fig. S9†). These findings suggested that CDs-API were highly effective in bacterial eradication and wound healing *in vivo*, demonstrating superior efficacy compared to ChA CDs alone. To evaluate the extent of inflammation, H&E staining was conducted on the infected wound tissues. The PBS group displayed extensive infiltration of inflammatory cells at the wound

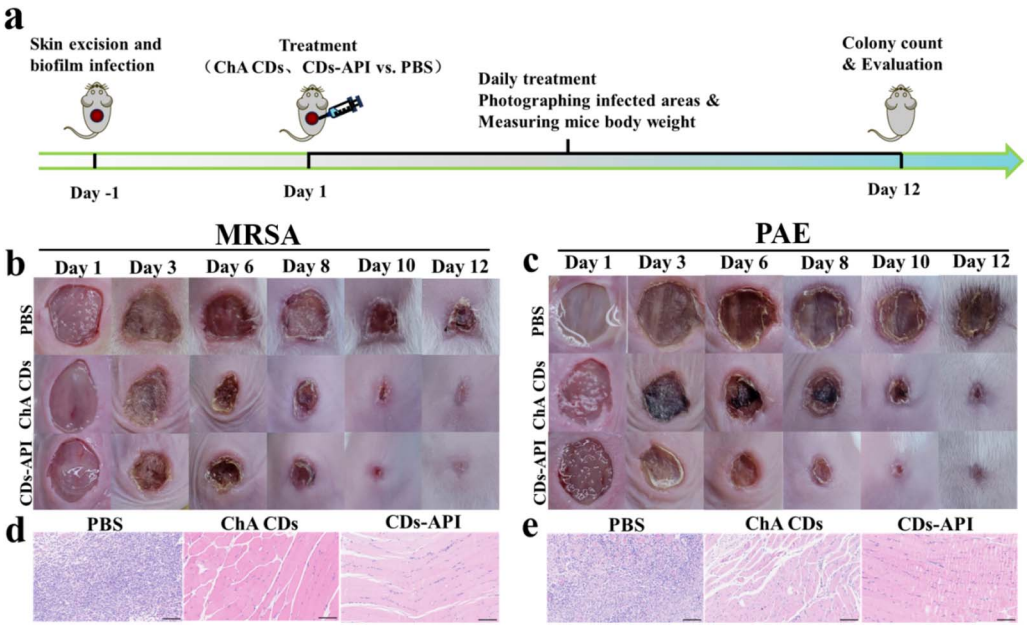

Fig. 5 Antibacterial performance evaluation of CDs-API*in vivo*. (a) Experimental timeline for the biofilm infection model mice. (b and c) Changes of infected areas in mice infected with MRSA and PAE. (d and e) H&E staining images of the infected skin areas after different treatments (scale bar: 100 μm).

site, while the ChA CDs and CDs-API groups showed a marked reduction inflammatory cell infiltration (Fig. 5d and e).

Additionally, no significant reduction in body weight was observed in any of these groups during the treatment period (Fig. S10†). Post-treatment, the major organs of the mice were surgically excised and subjected to H&E staining. The histological analysis revealed that the organs of mice in both the ChA CDs and CDs-API groups maintained normal morphological structures, with no observable toxic damage or histological alterations (Fig. S11†). These findings further substantiated the efficacy and biocompatibility of CDs-API as an antibacterial agent, underscoring their potential for clinical application.

Research on the antibacterial mechanism of CDs-APIs

Finally, we conducted a systematic investigation into the antibacterial mechanism of CDs-API. TEM results indicated MRSA and PAE cells treated with CDs-API exhibited significant shrinkage, collapse, and even rupture of the cell wall and membrane, as denoted by red arrows. Additionally, visible leakages of intracellular contents were observed (Fig. 6a). This damage to the cell membrane system often leads to alterations in bacterial membrane permeability and membrane potential. Consequently, we employed PI and $diSC_3(5)$ to further assess the extent of membrane damage. The fluorescence intensity of MRSA and PAE bacterial suspensions treated with CDs-API exhibited a significant increase following co-incubation with PI, with this enhancement being time-dependent (Fig. 6b). This observation suggested that the membrane damage induced by CDs-API resulted in increased permeability, hereby facilitating the entry of PI into the cells. Additionally, the $diSC_3(5)$ accumulates within the phospholipid bilayer, where it experiences fluorescence quenching. Upon alteration of the bacterial membrane potential, $diSC_3(5)$ was released, leading to the restoration of fluorescence. The $diSC_3(5)$ assay results showed a significant increase in fluorescence intensity in the presence of CDs-API (Fig. 6c), thereby confirming an alteration in bacterial membrane potential. These results indicated that CDs-API could disrupt the bacterial membrane system, affecting its integrity, permeability, and membrane potential. Furthermore, we evaluated the impact of this membrane damage on bacterial metabolic activity. Given that adenosine triphosphate (ATP) is a crucial component of bacterial energy metabolism, a reduction in ATP levels is generally indicative of diminished metabolic activity. Our study revealed a significant reduction in ATP content in the CDs-API group compared to the PBS group, suggesting that CDs-API could inhibit bacterial metabolic activity, potentially contributing to bacterial death (Fig. 6d). Additionally, the accumulation of ROS resulting from the GPX-like enzymatic activity of CDs-API could damage membrane proteins, nucleic acids, and various enzymes, thereby impeding bacterial proliferation. The generation of ROS in MRSA and PAE suspensions in the presence of CDs-API was further corroborated using the standard ROS indicator ABDA. The results showed that ChA CDs and CDs-API could promote the generation of ROS, and the amount of ROS increased over time (Fig. 6e). Considering the substantial presence of proteins and nucleic acids within biofilms, the biofilm disruption capability of CDs-API might be attributed to the accumulation of ROS. Although the ROS generation being comparable to that of ChA CDs, the enhanced antibacterial efficacy of CDs-API indicated the involvement of additional antibacterial mechanisms.

In summary, CDs-API exhibited the antibacterial effects through multiple pathways, including the disruption of cell

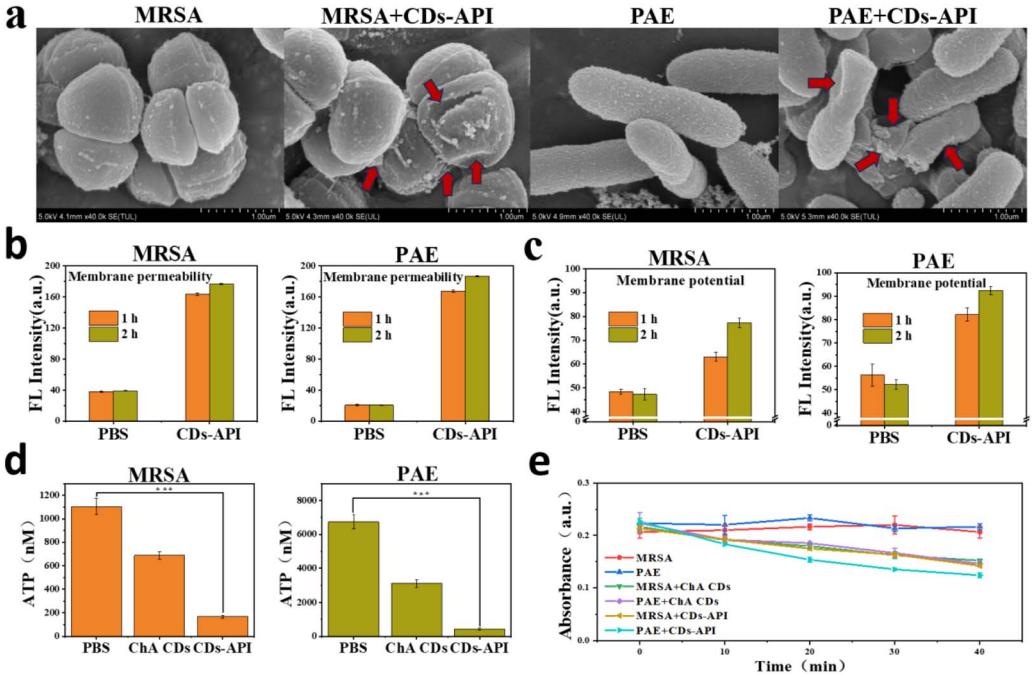

Fig. 6 Antibacterial mechanism of CDs-API. (a) SEM images of MRSA and PAE (scale bars: 1 μm). (b) Fluorescence intensity of PI in MRSA and PAE. (c) Fluorescence intensity of $diSC_3(5)$ in MRSA and PAE. (d) ATP level of MRSA and PAE treated with different groups. (e) Generation of ROS verified by monitoring the absorbance decrease of ABDA at 378 nm along with time increase (***$p < 0.001$).

membrane structure, alteration of membrane permeability, inhibition of metabolic activity, and promotion of ROS accumulation.

Conclusion

Our study had successfully designed and synthesized an innovative environmentally sensitive charge-switchable antimicrobial material, whose superior antibacterial properties had been effectively validated through both *in vivo* and *in vitro* studies. This material integrated the potent bactericidal efficacy characteristic of positively charged substances with the favorable biocompatibility associated with negatively charged materials. This dual functionality was achieved by modifying the surface of small-sized ChA CDs with an acid-responsive charge-converting imidazolyl group. Given that all enzyme-mimetic activities of nanozymes are fueled by electron transfer processes occurring at their surfaces,[62] the persistence of enzyme-like activity in CDs-API indicates that the incorporation of the small molecule modification did not disrupt the charge transfer mechanism inherent to the surface of ChA CDs. The enhanced fluorescence properties achieved through the effective passivation of surface defects in ChA CDs by API,[63] underscores the promising potential of small molecule modification in optimizing the performance characteristics of CDs. The GPX-like activity of CDs-API was confirmed to facilitate the consumption of GSH within biofilms, thereby promoting the accumulation of ROS and disrupting the bacterial redox equilibrium, ultimately inducing oxidative stress. Subsequent investigations into the antibacterial mechanism demonstrated that CDs-API could inhibit bacterial proliferation by compromising the integrity of the bacterial membrane system and disrupting bacterial metabolic processes. Notably, CDs-API demonstrates exceptional disruption efficacy against mature biofilms, presenting a viable option for the management of persistent and recurrent infections.[64] *In vivo* trials further substantiated that CDs-API effectively treated wound infections, enhanced wound healing, and inhibited bacterial growth at infection sites within a short period. Furthermore, CDs-API exhibited potent broad-spectrum antibacterial activity and hold significant potential for the treatment of various clinically prevalent drug-resistant bacterial infections. This conventional antibiotic alternative approach may prove more advantageous and present greater application opportunities in mitigating bacterial drug resistance.

Data availability

The data that support the findings of this study are available in this published article.

Ethics approval and consent to participate

All experiments were performed in compliance with relevant laws or guidelines and were followed institutional guidelines. All animal procedures were performed in accordance with the Guidelines for Care and Use of Laboratory Animals of Chongqing Medical University and approved by the Institutional Animal Care and Use Committee of Chongqing Medical University (IACUC-CQMU).

Consent for publication

We declare that this manuscript is original, has not been published before. We authorize the publication of this manuscript.

Author contributions

LZ and LH performed the *in vitro* and *in vivo* studies, curated the data, and wrote the original draft. TZR provided financial support. TQX and LC conducted the formal analysis. WD and TH designed this study, WD reviewed the manuscript. All authors read and approved the final manuscript.

Conflicts of interest

The authors declare that they have no competing interests.

Acknowledgements

We gratefully acknowledge the financial support provided by the Natural Science Foundation of Chongqing, China (CSTB2024NSCQ-MSX0202).

References

1 Antimicrobial Resistance Collaborators, Global burden of bacterial antimicrobial resistance in 2019: a systematic analysis, *Lancet*, 2022, **399**(10325), 629–655.
2 C. Willyard, The drug-resistant bacteria that pose the greatest health threats, *Nature*, 2017, **543**(7643), 15.
3 B. Malik and S. Bhattacharyya, Antibiotic drug-resistance as a complex system driven by socio-economic growth and antibiotic misuse, *Sci. Rep.*, 2019, **9**(1), 15184.
4 W. J. Caputo, P. Monterosa and D. Beggs, Antibiotic misuse in wound care: can bacterial localization through fluorescence imaging help?, *Diagnostics*, 2022, **12**(12), 3207.
5 Y. Shao, Y. Wang, Y. Yuan, *et al.*, A systematic review on antibiotics misuse in livestock and aquaculture and regulation implications in China, *Sci. Total Environ.*, 2021, **798**, 149205.
6 C. R. MacNair, S. T. Rutherford and M. W. Tan, Alternative therapeutic strategies to treat antibiotic-resistant pathogens, *Nat. Rev. Microbiol.*, 2024, **22**(5), 262–275.
7 P. Gupta, S. Sarkar, B. Das, *et al.*, Biofilm, pathogenesis and prevention–a journey to break the wall: a review, *Arch. Microbiol.*, 2016, **198**(1), 1–15.
8 Z. Pang, R. Raudonis, B. R. Glick, *et al.*, Antibiotic resistance in *Pseudomonas aeruginosa*: mechanisms and alternative therapeutic strategies, *Biotechnol. Adv.*, 2019, **37**(1), 177–192.
9 H. Wu, C. Moser, H. Z. Wang, *et al.*, Strategies for combating bacterial biofilm infections, *Int. J. Oral Sci.*, 2015, **7**(1), 1–7.
10 M. Zhou, Q. J. Cai, C. N. Zhang, *et al.*, Antibiotic resistance bacteria and antibiotic resistance genes survived from the extremely acidity posing a risk on intestinal bacteria in an *in vitro* digestion model by horizontal gene transfer, *Ecotoxicol. Environ. Saf.*, 2022, **247**, 114247.
11 R. Vivas, A. Barbosa, S. Dolabela, *et al.*, Multidrug-resistant bacteria and alternative methods to control them: an overview, *Microb. Drug Resist.*, 2018, **25**, 890–908.
12 X. Y. Li, D. M. Chen and S. Y. Xie, Current progress and prospects of organic nanoparticles against bacterial biofilm, *Adv. Colloid Interface Sci.*, 2021, **294**, 102475.
13 J. M. V. Makabenta, A. Nabawy, C. H. Li, *et al.*, Nanomaterial-based therapeutics for antibiotic- resistant bacterial infections, *Nat. Rev. Microbiol.*, 2021, **19**(1), 23–36.
14 M. Xie, M. Gao, Y. Yun, *et al.*, Antibacterial nanomaterials: mechanisms, impacts on antimicrobial resistance and design principles, *Angew Chem. Int. Ed. Engl.*, 2023, **62**(17), e202217345.
15 B. Mubeen, A. N. Ansar, R. Rasool, *et al.*, Nanotechnology as a novel approach in combating microbes providing an alternative to antibiotics, *Antibiotics*, 2021, **10**(12), 1473.
16 M. Alavi and A. Nokhodchi, A. Micro- and nanoformulations of antibiotics against Brucella, *Drug Discovery Today*, 2023, **28**(12), 103809.
17 S. Fu, X. Zhao, L. Yang, *et al.*, A novel Ti–Au alloy with strong antibacterial properties and excellent biocompatibility for biomedical application, *Biomater. Adv.*, 2022, **133**, 112653.
18 R. Qian, Z. Xu, X. Hu, *et al.*, Ag/Ag_2O with NIR-triggered antibacterial activities: photocatalytic sterilization enhanced by low-temperature photothermal effect, *Int. J. Nanomed.*, 2023, **18**, 1507–1520.
19 M. Busila, V. Musat, P. Alexandru, *et al.*, Antibacterial and photocatalytic activity of ZnO/Au and ZnO/Ag nanocomposites, *Int. J. Mol. Sci.*, 2023, **24**(23), 16939.
20 S. V. Gudkov, D. E. Burmistrov, V. V. Smirnova, *et al.*, A mini review of antibacterial properties of Al_2O_3 nanoparticles, *Nanomaterials*, 2022, **12**(15), 2635.
21 E. Lee, M. Lee, S. Kwon, *et al.*, Systematic and mechanistic analysis of AuNP-induced nanotoxicity for risk assessment of nanomedicine, *Nano Convergence*, 2022, **9**(1), 27.
22 P. Xiong, X. Huang, N. Ye, *et al.*, Cytotoxicity of metal-based nanoparticles: from mechanisms and methods of evaluation to pathological manifestations, *Adv. Sci.*, 2022, **9**(16), e2106049.
23 M. Wang, Y. Su, Y. Liu, *et al.*, Antibacterial fluorescent nano-sized lanthanum-doped carbon quantum dot embedded polyvinyl alcohol for accelerated wound healing, *J. Colloid Interface Sci.*, 2022, **608**(Pt 1), 973–983.
24 X. Wei, X. Wang, Y. Fu, *et al.*, Emerging trends in CDs@hydrogels composites: from materials to applications, *Mikrochim. Acta*, 2024, **191**(6), 355.
25 S. Chai, L. Zhou, Y. Chi, *et al.*, Enhanced antibacterial activity with increasing P doping ratio in CQDs, *RSC Adv.*, 2022, **12**(43), 27709–27715.
26 X. Xu, R. Ray, Y. Gu, *et al.*, Electrophoretic analysis and purification of fluorescent single-walled carbon nanotube fragments, *J. Am. Chem. Soc.*, 2004, **126**(40), 12736–12737.
27 Y. Zhang, P. Li, H. Yan, *et al.*, Green synthesis and multifunctional applications of nitrogen-doped carbon quantum dots *via* one-step hydrothermal carbonization of *Curcuma zedoaria*, *Anal. Bioanal. Chem.*, 2023, **415**(10), 1917–1931.

28 N. H. Hussen, A. H. Hasan, Y. M. Faqi Khedr, *et al.*, Carbon dot based carbon nanoparticles as potent antimicrobial, antiviral, and anticancer agents, *ACS Omega*, 2024, **9**(9), 9849–9864.
29 S. Mishra, K. Das, S. Chatterjee, *et al.*, Facile and green synthesis of novel fluorescent carbon quantum dots and their silver heterostructure: an *in vitro* anticancer activity and imaging on colorectal carcinoma, *ACS Omega*, 2023, **8**(5), 4566–4577.
30 Y. Feng, K. Wu, S. Wu, *et al.*, Carbon Quantum Dots-Derived Carbon Nanosphere Coating on Ti_3C_2 MXene as a Superior Anode for High-Performance Potassium-Ion Batteries, *ACS Appl. Mater. Interfaces*, 2023, **15**(2), 3077–3088.
31 V. Manikandan and N. Y. Lee, Green synthesis of carbon quantum dots and their environmental applications, *Environ. Res.*, 2022, **212**(Pt B), 113283.
32 X. Li, H. Wang, Y. Shimizu, *et al.*, Preparation of carbon quantum dots with tunable photoluminescence by rapid laser passivation in ordinary organic solvents, *Chem. Commun.*, 2011, **47**(3), 932–934.
33 D. Iannazzo, A. Pistone, S. Ferro, *et al.*, Graphene quantum dots based systems as HIV inhibitors, *Bioconjugate Chem.*, 2018, **29**(9), 3084–3093.
34 L. Gutiérrez-Gálvez, T. García-Mendiola, C. Gutiérrez-Sánchez, *et al.*, Carbon nanodot-based electrogenerated chemiluminescence biosensor for miRNA-21 detection, *Mikrochim. Acta*, 2021, **188**(11), 398.
35 Y. Zhang, C. Lei, P. Dong, *et al.*, Green synthesis of carbon dots from fish scales for selective turn off-on detection of glutathione, *RSC Adv.*, 2024, **14**(5), 3578–3587.
36 N. Nammahachak, K. K. Aup-Ngoen, P. Asanithi, *et al.*, Hydrothermal synthesis of carbon quantum dots with size tunability *via* heterogeneous nucleation, *RSC Adv.*, 2022, **12**(49), 31729–31733.
37 K. Dehvari, S. H. Chiu, J. S. Lin, *et al.*, Heteroatom doped carbon dots with nanoenzyme like properties as theranostic platforms for free radical scavenging, imaging, and chemotherapy, *Acta Biomater.*, 2020, **114**, 343–357.
38 Y. Y. Yao, G. Gedda, W. M. Girma, *et al.*, Magnetofluorescent Carbon Dots Derived from Crab Shell for Targeted Dual-Modality Bioimaging and Drug Delivery, *ACS Appl. Mater. Interfaces*, 2017, **9**(16), 13887–13899.
39 C. Dong, Y. Wang, T. Chen, *et al.*, Carbon Dots in the Pathological Microenvironment: ROS Producers or Scavengers?, *Adv. Healthcare Mater.*, 2024, e2402108.
40 J. Kaur, M. Bhattu, M. Rawat, *et al.*, Facile synthesis of carbon quantum dot/silver nanocomposite and its antimicrobial, catalytic and sensing applications, *Environ. Res.*, 2023, **237**(Pt 1), 116919.
41 C. Mou, X. Wang, Y. Liu, *et al.*, A robust carbon dot-based antibacterial CDs-PVA film as a wound dressing for antibiosis and wound healing, *J. Mater. Chem. B*, 2023, **11**(9), 1940–1947.
42 D. Guo, J. H. Lei, D. Rong, *et al.*, Photocatalytic Pt(IV)-coordinated carbon dots for precision tumor therapy, *Adv. Sci.*, 2022, **9**(36), e2205106.
43 M. G. Giordano, G. Seganti, M. Bartoli, *et al.*, An Overview on Carbon Quantum Dots Optical and Chemical Features, *Molecules*, 2023, **28**(6), 2772.
44 A. Truskewycz, H. Yin, N. Halberg, *et al.*, Carbon Dot Therapeutic Platforms: Administration, Distribution, Metabolism, Excretion, Toxicity, and Therapeutic Potential, *Small*, 2022, **18**(16), e2106342.
45 J. Huang, M. Xie, L. He, *et al.*, Chlorogenic acid: a review on its mechanisms of anti-inflammation, disease treatment, and related delivery systems, *Front. Pharmacol*, 2023, **14**, 1218015.
46 L. Yao, M. M. Zhao, Q. W. Luo, *et al.*, Carbon quantum dots-based nanozyme from Coffee Induces cancer cell ferroptosis to activate antitumor immunity, *ACS Nano*, 2022, **16**(6), 9228–9239.
47 C. Mou, X. Wang, Y. Liu, *et al.*, Positively charged BODIPY@carbon dot nanocomposites for enhanced photomicrobicidal efficacy and wound healing, *J. Mater. Chem. B*, 2022, **10**(39), 8094–8099.
48 X. Dai, Q. Xu, L. Yang, *et al.*, pH-responsive fluorescent polymer-drug system for real-time detection and *in situ* eradication of bacterial biofilms, *ACS Biomater. Sci. Eng.*, 2022, **8**(2), 893–902.
49 X. Chen, R. Guo, C. Wang, *et al.*, On-demand pH-sensitive surface charge-switchable polymeric micelles for targeting *Pseudomonas aeruginosa* biofilms development, *J. Nanobiotechnol.*, 2021, **19**(1), 99.
50 R. S. Kalhapure, M. Jadhav, S. Rambharose, *et al.*, pH-responsive chitosan nanoparticles from a novel twin-chain anionic amphiphile for controlled and targeted delivery of vancomycin, *Colloids Surf. B Biointerfaces*, 2017, **158**, 650–657.
51 Y. Ma, H. Xu, B. Sun, *et al.*, pH-Responsive Oxygen and Hydrogen Peroxide Self-Supplying Nanosystem for Photodynamic and Chemodynamic Therapy of Wound Infection, *ACS Appl. Mater. Interfaces*, 2021, **13**(50), 59720–59730.
52 Z. Han, M. Yuan, L. Liu, *et al.*, pH-Responsive wound dressings: advances and prospects, *Nanoscale Horiz.*, 2023, **8**(4), 422–440.
53 Y. Song, Y. Sun, M. Tang, *et al.*, Polyoxometalate modified by zeolite imidazole framework for the pH-responsive electrodynamic/chemodynamic Therapy, *ACS Appl. Mater. Interfaces*, 2022, **14**(4), 4914–4920.
54 S. W. Park, T. E. Kim and Y. K. Jung, Glutathione-decorated fluorescent carbon quantum dots for sensitive and selective detection of levodopa, *Anal. Chim. Acta*, 2021, **1165**, 338513.
55 T. Pan, H. Chen, X. Gao, *et al.*, Engineering efficient artificial nanozyme based on chitosan grafted Fe-doped-carbon dots for bacteria biofilm eradication, *J. Hazard. Mater.*, 2022, **435**, 128996.
56 X. He, L. Dai, L. Ye, *et al.*, A vehicle-free antimicrobial polymer hybrid gold nanoparticle as synergistically therapeutic platforms for *Staphylococcus aureus* infected wound healing, *Adv. Sci.*, 2022, **9**(14), e2105223.
57 E. G. Di-Domenico, A. Oliva and M. Guembe, The current knowledge on the pathogenesis of tissue and medical

device-related biofilm infections, *Microorganisms*, 2022, **10**(7), 1259.

58 X. S. Li, J. Z. Xue, Y. Qi, *et al.*, Citric Acid confers broad antibiotic tolerance through alteration of bacterial metabolism and oxidative stress, *Int. J. Mol. Sci.*, 2023, **24**(10), 9089.

59 F. Li, Y. Du, J. Liu, *et al.*, Responsive Assembly of Upconversion Nanoparticles for pH-Activated and Near-Infrared-Triggered Photodynamic Therapy of Deep Tumors, *Adv. Mater.*, 2018, **30**(35), e1802808.

60 P. Li, S. Liu, G. Zhang, *et al.*, Design of pH-Responsive Dissociable Nanosystem Based on Carbon Dots with Enhanced Anti-biofilm Property and Excellent Biocompatibility, *ACS Appl. Bio Mater.*, 2020, **3**(2), 1105–1115.

61 M. Ghirardello, J. Ramos-Soriano and M. C. Galan, Carbon Dots as an Emergent Class of Antimicrobial Agents, *Nanomaterials*, 2021, **11**(8), 1877.

62 G. Xu, K. Liu, B. Jia, *et al.*, Electron Lock Manipulates the Catalytic Selectivity of Nanozyme, *ACS Nano*, 2024, **18**(4), 3814–3825.

63 Y. Li, M. Deng, X. Zhang, L. Qian and C. Xiang, Proton-Prompted Ligand Exchange to Achieve High-Efficiency $CsPbI_3$ Quantum Dot Light-Emitting Diodes, *Nanomicro Lett.*, 2024, **16**(1), 105.

64 C. Shu, W. Zhang, Y. Zhang, *et al.*, Copper-Bearing Metal–Organic Framework with Mucus-Penetrating Function for the Multi-Effective Clearance of Mucosal Colonized Helicobacter pylori, *Research*, 2024, **7**, 0358.